

## Predicting the weld zones size in FSSW of 304L stainless steel plates by mathematical model based on RSM

Amir Hossein Daei-Sorkhabi

Department of Mechanical Engineering, Tabriz Branch, Islamic Azad University, Tabriz, Iran,

(\*Corresponding author: [amirsorkhabi@iaut.ac.ir](mailto:amirsorkhabi@iaut.ac.ir))

Submitted: 16 October 2022; Accepted: 30 May 2023; Available On-line: 31 October 2023

**ABSTRACT:** The 300 series austenitic stainless steels are widely used in industries due to their special properties. High heat in fusion welding reduces the properties of these steels and causes many problems. Therefore, stir friction spot welding, which is a type of solid state welding, is useful and widely used in high-tech industries. In this paper, a 3D dynamic explicit finite element model is developed to simulate the friction stir spot welding of 304L stainless steel plates. Using this model, the temperature distribution and the size of weld zones (thickness of weld zones) are obtained. Then, by experimental study, the results of the temperature and the size of weld zones were obtained to be a criterion for comparing and validating the numerical results. Microstructure and hardness of these zones are determined experimentally. Finally, a mathematical model based on the response surface methodology is proposed to predict the size of weld zones. Good agreement between the numerical results that are produced by the finite element simulation, the proposed model and the experimental data is observed. The results show the maximum temperature level appears in the stir zone and it reduces by moving from the weld center. Also, by increasing the rotational speed, plunging depth and dwell time of the tool, the size of both the stir zone and the heat affected zone increase to a peak value and then the size of the latter zone decreases.

**KEYWORDS:** 304L stainless steel; Design of experiments; Finite element method; Friction stir spot welding response surface methodology; Weld zone size

Citation/Citar como: Daei-Sorkhabi, A.H. (2023). "Predicting the weld zones size in FSSW of 304L stainless steel plates by mathematical model based on RSM". *Rev. Metal.* 59(2): e240. <https://doi.org/10.3989/revmetalm.240>

**RESUMEN:** *Predicción del tamaño de las zonas de soldadura usando soldadura por fricción-agitación de punto de placas de acero inoxidable 304L mediante un modelo matemático basado en la metodología de superficie de respuesta.* Los aceros inoxidables austeníticos de la serie 300 son ampliamente utilizados en la industria debido a sus propiedades especiales. El alto calor aplicado en la soldadura por fusión reduce las propiedades de estos aceros y causa muchos problemas. Por esta razón, la soldadura por fricción-agitación de punto, que es un tipo de soldadura en estado sólido, es útil y se utiliza ampliamente en las industrias de alta tecnología. En este trabajo, se desarrolla un modelo de elementos finitos explícito y dinámico en 3D para simular la soldadura por fricción-agitación de punto de placas de acero inoxidable 304L. Utilizando este modelo, se obtienen la distribución de la temperatura y el tamaño de las zonas de soldadura (espesor de las zonas de soldadura). A continuación,

**Copyright:** © 2023 CSIC. This is an open-access article distributed under the terms of the Creative Commons Attribution 4.0 International (CC BY 4.0) License.

mediante un estudio experimental, se obtienen los resultados de la temperatura y el tamaño de las zonas de soldadura para que sirvan de criterio de comparación y validación de los resultados numéricos. La microestructura y la dureza de estas zonas se determinan experimentalmente. Por último, se propone un modelo matemático basado en la metodología de superficie de respuesta para predecir el tamaño de las zonas de soldadura. Se observa una buena correlación entre los resultados numéricos que arroja la simulación por elementos finitos, el modelo propuesto y los datos experimentales. Los resultados muestran que el nivel máximo de temperatura aparece en la zona de agitación y se reduce al alejarse del centro de la soldadura. Asimismo, al aumentar la velocidad de giro, la profundidad de penetración y el tiempo de permanencia de la herramienta, el tamaño tanto de la zona de agitación como de la zona afectada por el calor aumenta hasta alcanzar un valor máximo y, a continuación, disminuye el tamaño de esta última zona.

**KEYWORDS:** Acero inoxidable 304L; Diseño de experimentos; Método de elementos finitos; Soldadura por fricción-agitación de punto; Tamaño de zona soldada

**ORCID ID:** Amir Hossein Daei-Sorkhabi (<https://orcid.org/0000-0002-3419-3379>)

## 1. INTRODUCTION

AISI-304L stainless steel is the most widely used alloy among the austenitic stainless steel commercial grades (Kondapalli *et al.*, 2014). It is used in mechanical equipment such as boilers and heat exchangers in petrochemical and power plants. 304L stainless steel (304L SS) is a low-carbon (~ 0.03 wt.% maximum carbon) type of 304 series in which the carbide precipitations are eliminated during the welding (Kondapalli *et al.*, 2014; Vakili Tahami *et al.*, 2010).

Friction stir welding (FSW) was invented at the welding institute of the UK in 1991 and was primarily used for joining the aluminum alloy plates (Mishra and Ma, 2005; Mohan and Wu, 2021). This method can be considered as a promising welding method for joining different type of metals and alloys which fusion welding is difficult (Heidarzadeh and Saeid, 2013; Verma *et al.*, 2022; Kheder *et al.*, 2023). It is fundamentally a solid state process without large distortion, solidification cracking, porosity, oxidation, and other defects that are outcomes of conventional fusion welding methods. Thus, FSW could produce the joints with better mechanical properties such as the ultimate tensile strength, ductility, and hardness compared with the joints that are welded by the conventional fusion welding processes (Mishra, 2008; Mohan and Wu, 2021; Sharabeyani and Daei Sorkhabi, 2022). Therefore, nowadays FSW is widely used in industry (Heidarzadeh *et al.*, 2021; Verma *et al.*, 2022). During FSW, a non-consumable rotating tool plunges into the plates and traverses along the weld line. The heat generated by the FSW tool and the plastic deformation cause work-pieces to join (Salih al *et al.*, 2023). Furthermore, friction stir spot welding (FSSW) as a new spot welding process, can be used to join the overlapping work-pieces and is a good replacement of the resistance spot welding (Reilly *et al.*, 2015). FSSW was initially limited to join aluminum plates due to the difficulty in selecting the appropriate tool materials that is capable of withstanding the high temperature during the joining process of the steels. However, by developing new technology and tool materials, this process can be

even applied to weld the stainless steel now (Aota and Ikeuchi, 2009; Lakshminarayanan *et al.*, 2015; Ahmed *et al.*, 2016). Hence the application of the FSW/FSSW on the stainless steels is the subject of recent studies, which provides important knowledge about the properties and microstructure of welded stainless steel parts by investigating various parameters (Reynolds *et al.*, 2003; Kokawa *et al.*, 2005; Park *et al.*, 2003; Siddiquee *et al.*, 2015; Ragab *et al.*, 2021; Siddiquee *et al.*, 2020). For example, Reynolds *et al.* (2003) have examined an initial assessment of the tensile properties, optical microstructure, and residual stress state of two friction stir welds in 304L SS. Kokawa *et al.* (2005) have investigated the details of the microstructural features, and the relationship between the hardness profile and the microstructure in friction stir welded 304 SS plates. Also, in the other work, Park *et al.* (2003) have shown that FSW of 304 SS using a polycrystalline cubic boron nitride tool causes the formation of sigma phase along the advancing side of the welding tool, and they proposed a theory for the evolution of sigma phase during the FSW. Ragab *et al.* (2021) have developed a 3D thermo-mechanical finite element model based on the Coupled Eulerian Lagrangian approach investigate FSW of martensitic stainless steel. Also, Siddiquee *et al.* (2020) have focused on butt-welding of AISI 304 stainless steel by friction stir welding. In this research the effect of the shoulder diameter, tool and traverse speed parameters have been investigated by using Taguchi's L27 orthogonal array.

Due to the generated heat and severe plastic deformation during the FSW, the method can be considered as a thermo-mechanical process. Therefore, the welding parameters such as tool rotational speed, travel speed, plunge depth, dwell time that control the final microstructure and mechanical properties of the welded joints. Vinayak *et al.* (2014) have investigated FSW and FSSW using ABAQUS/Explicit based on the finite element method (FEM). They have also studied the effect of parameters and tool geometry on temperature and morphology of the weld region. They have shown that the shape of the tool has an effect on the generated heat. The square and triangular pin profiles of the tool increase the

temperature of the process compared to the circular pin profiles. Also, the solution time is reduced to a greater extent by using Coupled Eulerian-Lagrangian method when compared to Lagrangian and Eulerian ones. Hirasawa *et al.* (2010) used a practical method to assess the effect of tool geometry on the plastic flow and material mixing during FSSW. They have shown that for high strength spot welds, triangular pin with a concave shoulder is the preferred tool geometry. Ravi Sekhar *et al.* (2018) studied the effect of the tool's rotational speed on the FSSW of AA5052-H38 aluminum alloy. They reached the maximum shear load of 4.215 kN. Bang *et al.* (2018) have investigated the mechanical properties of dissimilar A356/SAPH440 lap joints with FSSW and Self-Piercing Riveting. They found that the maximum shear load values in the weld joints is approximately 3.5 and 7.9 kN in self-piercing riveting joints. Avinash *et al.* (2014) investigated the feasibility of FSW of AA7075 T6 and AA2024 T3 dissimilar aluminum alloys. They also studied the mechanical properties of the weldment. The effects of the tool rotational speed and the welding speed on the joint performance were analysed in this paper. The FSW of EH46 steel was investigated by Al-Moussawi *et al.* (2017). They studied the impact of the welding parameters including the tool rotational speed and plunge depth in dwell stage on the weld zone microstructure. They found that a small increase in the plunge depth causes a significant change in the microstructure, and also increasing the tool rotational speed leads to a significant difference in the microstructure.

The literature review reveals that there is a need to develop a relationship relating the mechanical properties of the FSSW joints to the welding parameters. This type of relations will be an ideal method in industry to predict the properties of the joint beforehand. Such relationships are developed in this paper and relate the rotational speed, plunge depth and dwell time to the thickness of the weld zones that in turn affect the mechanical properties of the joint. Considering the extensive use of the austenitic 304L SS in different industries, the effect of welding parameters on the

thickness of weld zones, which is called the size of the weld zones, and the temperature distribution of FSSW of 304L SS plates is studied in this paper. The FSSW process is modeled based on the FEM numerical solution and a three dimensional dynamic thermo-mechanical modeling has been used for predicting the temperature history in the welded plates and the size of weld zones. Then, a set of experimental data is obtained for comparing and validating the numerical results. The FSSW tests have been conducted based on the design of experiments (DOE) and then in order to optimize and study the influence of the tool rotational speed, plunging depth and dwell time on the temperature distribution and the size of the weld zones, the Response Surface Methodology (RSM) has been applied to propose a mathematical model.

## 2. MATERIALS AND METHODS

### 2.1. Material specification

The chemical composition of 304L SS is given in Table 1 and its temperature-dependent physical and mechanical properties are shown in Table 2.

TABLE 1. The chemical composition of 304L SS (wt. %) (Vakili Tahami *et al.*, 2010)

| C    | Si  | Mn  | P    | Cr   | Mo  | Ni  | Co   | Cu  | Fe   |
|------|-----|-----|------|------|-----|-----|------|-----|------|
| 0.03 | 0.4 | 1.4 | 0.01 | 18.1 | 0.2 | 8.6 | 0.18 | 0.4 | 70.4 |

### 2.2. Response Surface Methodology (RSM)

The main aim of DOE is to identify the points/conditions where the experiments should be carried out or evaluated. After collecting a large set of experimental data, several techniques can be used to fit these data; and then, they may also be used in the numerical solutions. The RSM is a mathematical and statistical

TABLE 2. Temperature-dependent physical and mechanical properties of 304L SS (Zhu and Chao, 2004)

| Temperature (°C) | Thermal conductivity (W/cm °C) | Specific heat capacity (J/g °C) | Thermal expansion coefficient (µm /m °C) | Yield stress* (MPa) | Elastic modulus (MPa) | Poisson's ratio (-) |
|------------------|--------------------------------|---------------------------------|--|---------------------|-----------------------|---------------------|
| 0                | 0.13                           | 0.455                           | 17.85                                    | 297.14              | 203.57                | 0.3                 |
| 200              | 0.15                           | 0.522                           | 17.86                                    | 257.14              | 196.42                | 0.3                 |
| 400              | 0.188                          | 0.533                           | 17.86                                    | 207.14              | 171.43                | 0.3                 |
| 600              | 0.22                           | 0.566                           | 17.86                                    | 178.57              | 157.14                | 0.3                 |
| 800              | 0.266                          | 0.577                           | 17.86                                    | 50                  | 135.71                | 0.3                 |
| 1000             | 0.266                          | 0.577                           | 17.86                                    | 28.57               | 135.71                | 0.3                 |

\* Yield stress for 0.2% offset

technique for DOE. An important feature of the RSM is the design of experiments. The aim of this technique is to optimize the test results that are affected by several independent variables (input variables). In fact, RSM assists in the selection of the appropriate experimental design and the definition of the tests. The application of the RSM also covers the mathematic–statistical treatment of the test data by fitting the polynomial function to them. In this line, Box et al. developed the RSM in early 50 s (Khuri and Mukhopadhyay, 2010). This method uses the fit of predefined models to the experimental results. For this purpose, linear or square polynomial relationships are implemented to explain the system studied and, subsequently, to identify (modeling and displacing) experimental parameters to obtain an optimum condition (Khuri and Mukhopadhyay, 2010). Usually a second-order model together with the two-level factorial design are used, but this method may fail if extra effects, such as second-order effects, are significant. In this case, a central point in two-level factorial designs is implemented to evaluate the relationship. The next step is to obtain the additional terms that explain the interaction between the different test parameters. Using the above techniques, the following polynomial known as Box–Behnken (Khuri and Mukhopadhyay, 2010) can be suggested:

$$y = \beta_0 + \sum_{i=1}^k \beta_i x_i + \sum_{i=1}^k \beta_{ii} x_i^2 + \sum_{1 \leq i < j \leq k} \beta_{ij} x_i x_j + \varepsilon \quad (1)$$

where  $k$  is the number of variables,  $\beta_0$  is the constant term,  $\beta_i$  are the polynomial coefficients,  $x_i$  refers to the variables,  $\beta_{ij}$  introduce the interaction between these variables and  $\varepsilon$  is the residual associated to the error in test results.

### 2.3. Numerical method

To capture the thermo-mechanical response under the given system and process parameters, coupled temperature and displacement numerical formulations are used along with the heat generation factor. The frictional heat generation formulation involves the calculation of the heat flux at the interface elements located on the contacting parts (tool and work-piece). The heat flux is applied as a thermal load to the volume of elements on each part. Thermal distributions to each surface are given in Equations (2) and (3):

$$q_{\text{tool}} = q_k + q_r - f_{\text{tool}} q_g \quad (2)$$

$$q_{\text{wp}} = -q_k - q_r - f_{\text{wp}} q_g \quad (3)$$

where,  $q_{\text{tool}}$  and  $q_{\text{wp}}$  are the thermal loads, the heat flux to the tool and the work-piece respectively,  $q_g$  is the total heat generated by the interface element due to the

friction,  $q_r$  is the heat flux due to the radiation,  $q_k$  is the heat flux due to the conduction, and  $f_{\text{tool}}$  and  $f_{\text{wp}}$  stand for the fraction of the total generated heat flux ( $q_g$ ) to the tool and the work-piece ( $q_{\text{tool}} + q_{\text{wp}} = 1$ ).

In order to incorporate the hardening effect due to the plastic deformation (as a function of applied temperature), Johnson Cook material constitutive model is employed. This model is mathematically given in Eq. (4), which is extensively used for extrusion, forging and impact analyses (Al-Moussawi *et al.*, 2017; Zhu and Chao, 2004; Khuri and Mukhopadhyay, 2010; Johnson and Cook, 1983):

$$\bar{\sigma} = [A + B(\bar{\varepsilon}^{\text{pl}})^n] \left[ 1 + C \ln \left( \frac{\dot{\varepsilon}^{\text{pl}}}{\dot{\varepsilon}_0} \right) \right] (1 - \hat{\theta}^m) \quad (4)$$

where  $\bar{\sigma}$  is the effective yield strength,  $\bar{\varepsilon}^{\text{pl}}$  is the equivalent plastic strain rate,  $\dot{\varepsilon}_0$  is a coefficient to normalize the strain rate,  $A$  is the yield stress constant,  $B$  is the strain hardening constant,  $n$  is the strain hardening exponent,  $C$  is the strain rate hardening constant and  $m$  is the temperature dependent coefficient. Also,  $\hat{\theta}$  presents the non-dimensional temperature, which is given as below (Al-Moussawi *et al.*, 2017; Zhu and Chao, 2004; Khuri and Mukhopadhyay, 2010; Johnson and Cook, 1983):

$$\hat{\theta} = \begin{cases} 0 & \theta < \theta_{\text{ref}} \\ \frac{\theta - \theta_{\text{ref}}}{\theta_{\text{melt}} - \theta_{\text{ref}}} & \theta_{\text{ref}} \leq \theta \leq \theta_{\text{melt}} \\ 1 & \theta > \theta_{\text{ref}} \end{cases} \quad (5)$$

where  $\theta$ ,  $\theta_{\text{ref}}$ ,  $\theta_{\text{melt}}$  are the current, reference and melting temperatures. Johnson Cook material constitutive parameters for 304L SS are presented in Table 3 (Maurel-Pantel *et al.*, 2012).

TABLE 3. Material parameters associated to the Johnson-Cook model for 304L SS (Maurel-Pantel *et al.*, 2012)

| A (MPa) | B (MPa) | C (-) | n (-)  | m (-) | $\theta_{\text{ref}}$ (°C) | $\theta_{\text{melt}}$ (°C) |
|---------|---------|-------|--------|-------|----------------------------|-----------------------------|
| 253.32  | 685.1   | 0.097 | 0.3128 | 2.044 | 23                         | 1425                        |

By employing the arbitrary lagrangian-eulerian (ALE) formulation, large deformations may be simulated by re-meshing the FE model in ABAQUS by “8-node C3D8RT” element Abaqus Version 6.14 (2014). The main point is to control the distortion of the elements by improving the aspect ratio of the distorted elements. This is done by the inter-step conversion of the results at the integration points and re-adjustment of the nodal positions as close as possible to the original coordinates. As compared to the pure Eulerian formulations, the advantage in using ALE formulation is that in the ALE approach the “free” surfaces have Lagrange

properties in the normal direction, in a way that the surface tracking and partially filled elements are avoided. Hence, the position of the surface of the domain is found directly by solving the governing equation and the iterations are not required (Al-Moussawi *et al.*, 2017). The FSSW geometry consists of three components including a rigid tool and two 304L SS plates. The dimensions of the plates and the tool location are given in Fig. 1.

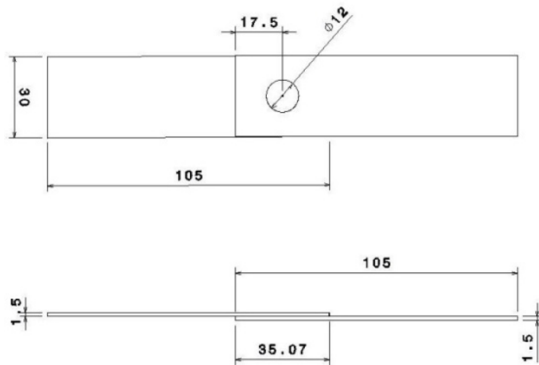


FIGURE 1. Dimensions of the welding plates (mm).

According to Fig. 2, boundary conditions are applied in the modeling as follows: upper and lower edges of the work-pieces are restrained and fixed in the horizontal direction; the welding tool has transitional and rotational movement. The convection coefficient of  $30 \text{ W/m}^2 \text{ } ^\circ\text{C}$  at  $25 \text{ } ^\circ\text{C}$  is applied to all surfaces that are exposed to the surrounding air (Awang, 2007; Jiji, 2006).

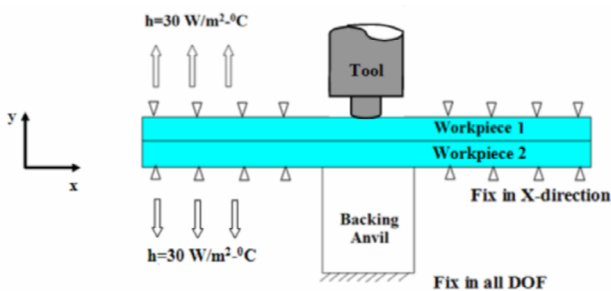


FIGURE 2. Schematic view a part of the model and boundary conditions.

#### 2.4. Experimental method

Two similar 304L SS plates are joined by FSSW process and the temperature levels of the selected points around the weld zone are measured during the welding process, and then, the microstructure, hardness and thickness of the weld zones are determined. The FSSW

tool, made of Tungsten Carbide, and its dimensions are shown in Fig. 3a and Fig. 3b, respectively.



FIGURE 3. a) Photograph of welding tool b) Dimensions of the welding tool (mm).

For the welding process, a Universal Milling Machine shown in Fig. 4a is used and Fig. 4b shows the plates are fixed by a set of fixtures during the welding. Fig. 4a and 4b show that the welding tool is installed on the spindle and rotates around the axis perpendicular to the surface of the plate. Welded plates are shown in Fig. 4c.

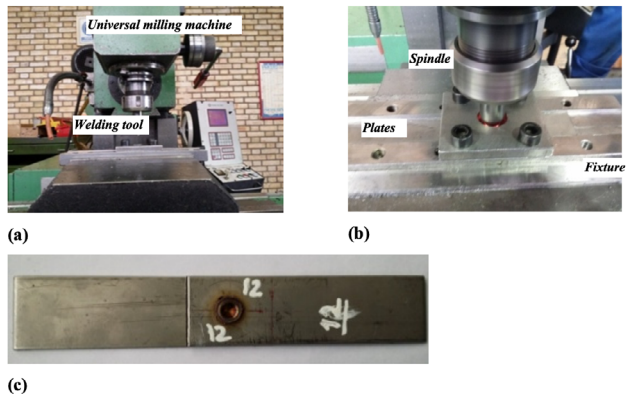


FIGURE 4. a) Welding equipment b) Fixed plates while being welded c) Specimen of welded plates.

An Axial force exerted by the milling machine head is applied to the material and welding is being possible by the extreme plastic deformation in the solid phase that includes recrystallization of the base material (BM), and eventually, a strong metallurgical connection is created. In this way, the stir zone (SZ), thermo-mechanical affected zone (TMAZ) and heat affected zone (HAZ) are formed around the weld spot. In order to study the microstructure of the welded specimens, macrographs are taken from the mid-plane perpendicular cross section of the weld zone according to ASTM E3-01 (2001). The marble solution with 50 ml hydrochloric acid, 50 ml distilled water and 10 g copper sulfate is used to etch the specimen's surface and the macro-graphic images of the specimens are taken using an optical microscope. Then, the surface hard-

ness of the specimens in different points of the weld cross section are determined based on ASTM E384 (2017) using Micro Vickers method.

Temperature of the points have been measured by a K type thermocouple during the FSSW process. These thermocouples are linked to a PC equipped with a data acquisition system through the digital thermometers (TM-747D) or analogue to digital converters indicating the temperature change/history during the process.

### 2.5. Design of experiment conditions by response surface method

Rotational speed of the tool, plunging depth and dwell time are selected as process variables in this research identifying the major parameters affecting the nugget of the FSSW and the structure of the weld zones. In order to study the effect of these parameters on the size of the weld zones, the tests are conducted based on DOE method and RSM has been used for proposing a model to predict the zone sizes. The mentioned parameters are considered as input data and three levels of them (given in Table 4) are selected.

TABLE 4. Welding parameters and their levels

| Parameters       | Notation | Units | Levels |     |      |
|------------------|----------|-------|--------|-----|------|
|                  |          |       | -1     | 0   | 1    |
| Plunging Depth   | P        | mm    | 0      | 0.1 | 0.2  |
| Dwell Time       | D        | s     | 1      | 4   | 7    |
| Rotational Speed | R        | rpm   | 500    | 750 | 1000 |

These levels are selected based on the previous experiences that produce appropriate joints and the reported values for the similar material (Lakshminarayanan *et al.*, 2015; Ahmed *et al.*, 2016). This set of input data is the foundation of the numerical and experimental analyses in this research.

## 3. RESULTS AND DISCUSSION

### 3.1. Microstructures

The cross section images of the FSSW for two 304L SS plates with magnification factor 50 (Mag. =50x) are shown in Fig. 5a. In this case, the tool rotational speed is 750 rpm, the plunging depth is 0.1 mm and the dwell time is 4 s. For better resolution, macrographs with Mag. = 200x are shown in Fig. 5b. Considering the structural characteristics, three weld zones: stir zone (SZ), thermo-mechanical affected zone (TMAZ) and heat affected zone (HAZ), can be seen in this figure. The procedure is repeated for all other case studies with different welding parameters listed in Table 4.

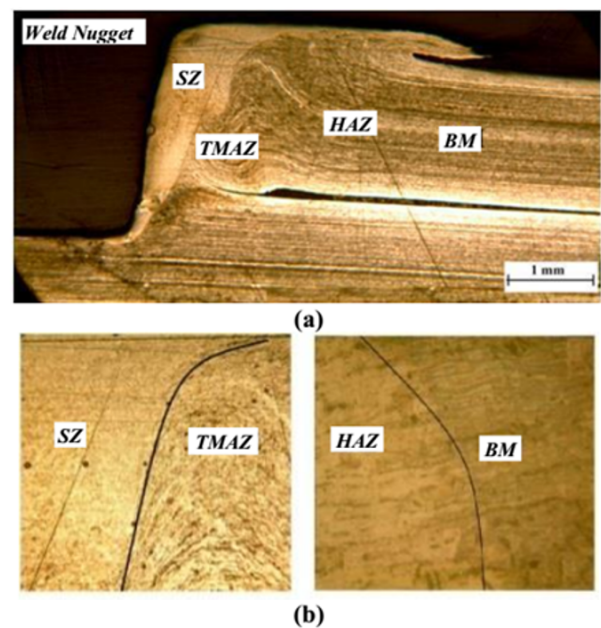


FIGURE 5. Macroscopic image of the welded zones a) macro X-Ray image, Mag. = 50x b) macro X-ray image, Mag. = 200x.

### 3.2. Hardness

In the present research, Vickers Hardness for different points on the plate surface along a radial line starting from the outer surface of the weld nugget has been investigated. Considering that the process of changes in the hardness-distance diagram is almost the same for all case studies, for example in Fig. 6, this process shown for case study with tool rotational speed: 750 rpm, dwell time: 4 s, and plunging depth: 0.1 mm. The vertical axis of this figure is located at the outer surface of the weld nugget. As shown in this figure, the SZ hardness is maximum (250 Vickers) and it decreases by moving away from this area. In other words, SZ has the highest amount of hardness. The reason for that is the microstructure of its fine grains, which can be clearly seen in this figure. It can also be caused by the plastic deformation as a result of pressure by the tool pin and work hardening phenomenon. By entering to the TMAZ, the amount of hardness is reduced due to the lower amount of plastic deformation or stir. In other words, the reason for which was low is the mixing and reduction of the effect of welding fineness in this zone. In the HAZ, the decreasing trend of the hardness continues to reach the base metal hardness, which is equal to 192 Vickers. The SZ hardness numbers for three case studies are presented in Table 5.

As it is shown in this figure, the SZ hardness is maximum (250 Vickers) and it decreases by moving away from this area. In other words, SZ has the highest hardness because of its microstructure. By entering in the TMAZ, the hardness is reduced due to the lower

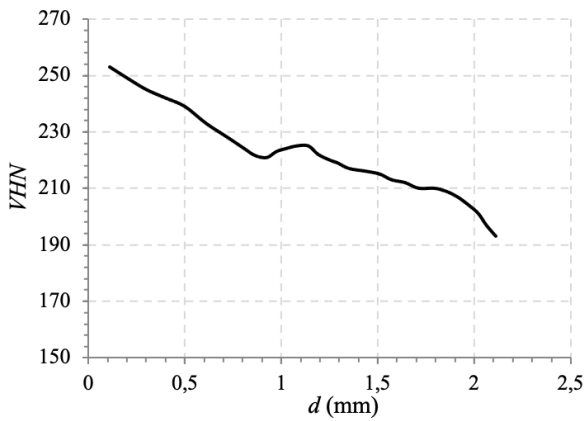


FIGURE 6. Vickers Hardness for different points on the plate surface along a radial line. The vertical axis is located at the outer surface of the weld nugget.

amount of plastic deformation or stir. In the HAZ, the decreasing trend of the hardness continues to reach the base metal hardness, which is equal to 192 Vickers. The SZ hardness numbers for three case studies are presented in Table 5.

TABLE 5. Experimentally measured data for maximum hardness (SZ hardness)

| Case study No. | Rotational speed (rpm) | Dwell time (s) | Plunging depth (mm) | Maximum hardness (SZ hardness) |
|----------------|------------------------|----------------|---------------------|--------------------------------|
| 1              | 500                    | 1              | 0                   | 220                            |
| 2              | 750                    | 4              | 0.1                 | 250                            |
| 3              | 1000                   | 7              | 0.2                 | 285                            |

### 3.3. Temperature distribution

Figure 7 shows the temperature distribution for the various weld zones in  $t=6$  s. It can be seen that SZ has the maximum temperature level (almost 1200 °C) due to the heat generated from the plastic stirring and friction. Temperature level history for three points (A, B and C) on the section mid line and in the different zones that are obtained using the FEM solutions are

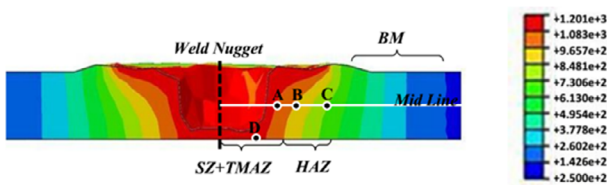


FIGURE 7. Temperature distribution in the weld nugget and different weld zones at  $t=6$  s.

shown in Fig. 8. In FEM simulation for this case study, the rotational speed of the tool, the plunging depth and the dwell time are 750 rpm, 0.1 mm and 4 s respectively. The difference in temperature level also affects the microstructure of the zones. Also, this figure shows the maximum temperatures difference of the various regions is approximately 200 °C.

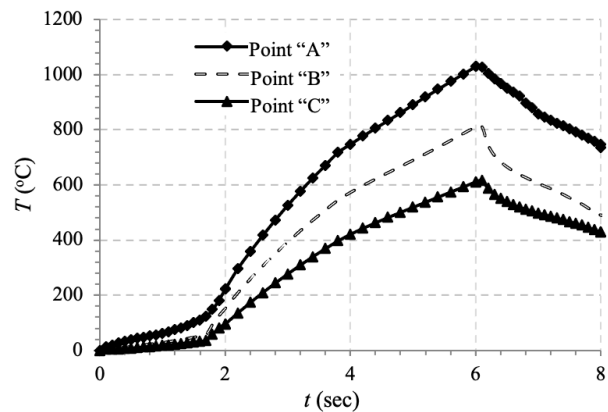


FIGURE 8. Temperature level history for different zones of FSS welded piece for case study 2.

For validating the FEM results, temperature levels of point “D” (see Fig. 7) have been measured. Fig. 9 shows the temperature history of both FE solution and experimental measurements for selected point (“D”).

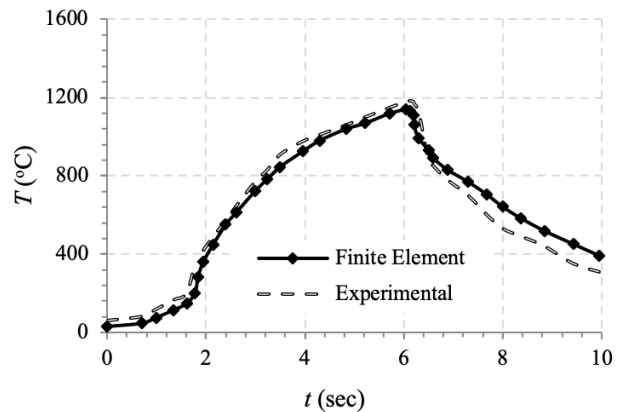


FIGURE 9. Temperature level history obtained by the experiment and FEM for point D (see Fig. 7) in case study 2.

In addition, the experimentally measured temperature levels are compared with those obtained using the FE solutions in Table 6. As it can be seen, there is a good agreement between the experimental data and the numerical results with maximum deviation of 40 °C (3.39%)

TABLE 6. FEM results and experimentally measured data for the maximum temperature of the weld zones

| Case study No. | Max. temperature of SZ (°C) |      |           | Max. temperature of TMAZ (°C) |      |           | Max. temperature of HAZ (°C) |      |           |
|----------------|-----------------------------|------|-----------|-------------------------------|------|-----------|------------------------------|------|-----------|
|                | FEM                         | Exp. | Error     | FEM                           | Exp. | Error     | FEM                          | Exp. | Error     |
| 1              | 1078                        | 1100 | 22(2%)    | 769                           | 788  | 19(2.41%) | 575                          | 592  | 17(2.87%) |
| 2              | 1140                        | 1180 | 40(3.39%) | 820                           | 831  | 11(1.32%) | 610                          | 619  | 9(1.45%)  |
| 3              | 1240                        | 1255 | 15(1.19%) | 876                           | 890  | 14(1.57%) | 670                          | 685  | 15(2.19%) |

### 3.4. Developing the mathematical model

As it was mentioned before, for studying the impact of the rotational speed (R), plunging depth (P) and dwell time (D) on the size of the weld zones, DOE conditions are determined by the RSM. Based on this method, fifteen tests are defined and conducted and their conditions are presented in Table 7.

Since carrying out these tests is expensive, the numerical model that has been validated in Section 3.3, is used to obtain the temperature distribution and the weld zone size for each case and their results are employed to develop a mathematical model by the RSM. The size of each zone is approximated based on their temperature level: between 1200 °C and 1000 °C is known as SZ+TMAZ and between 1000 °C and 850 °C for HAZ. Based on these data an order- two polynomial have been developed using the RSM to predict the

weld zone size for FSSW of 304 SS plates according to the selected operating conditions as below:

$$\begin{aligned} \text{size (SZ + TMAZ)} &= 0.000002R^2 + 0.00995D^2 - 4.79P^2 - 0.000200RD \\ &- 0.00350RP - 0.417DP - 0.001225R + 0.1662D + 6.81P \\ &+ 0.330 \end{aligned} \quad (6)$$

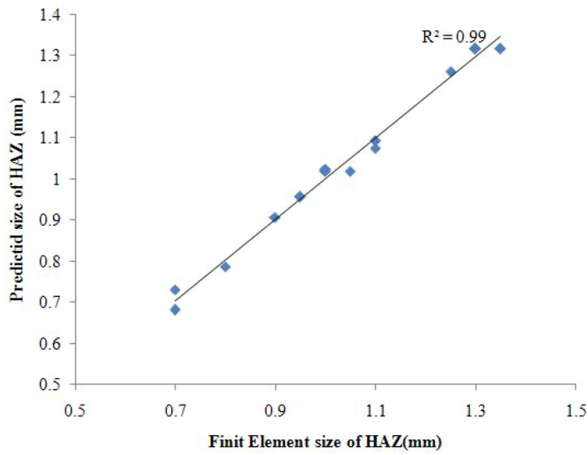
$$\begin{aligned} \text{size (HAZ)} &= -0.000002R^2 - 0.01412D^2 - 23.96P^2 - 0.000017RD \\ &- 0.003000RP - 0.2500DP + 0.004542R + 0.1859D + 8.417P \\ &- 1.466 \end{aligned} \quad (7)$$

### 3.5. Validation of the mathematical model

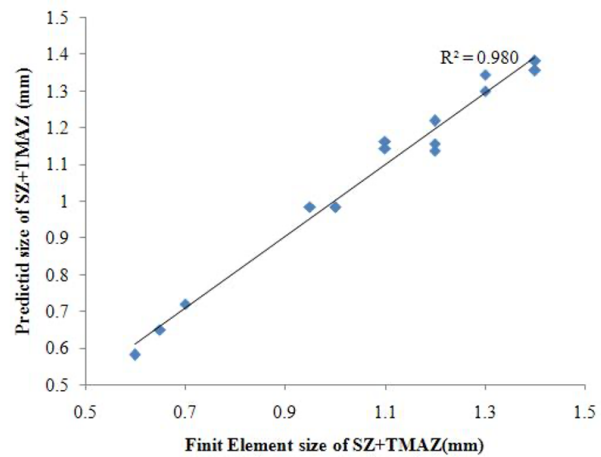
In Fig. 10 and Fig. 11 the results obtained from the finite element model and the mathematical model for the size of HAZ and SZ+TMAZ are compared. According to the  $R^2$  values (>95%), it can be seen

TABLE 7. Input and output parameters in DOE

| Test number | level   | Rotational speed (rpm) | Dwell time (s) | Plunging depth (mm) | Thickness of SZ+TMAZ (mm) | Thickness of HAZ (mm) |
|-------------|---------|------------------------|----------------|---------------------|---------------------------|-----------------------|
| 1           | -1 -1 0 | 500                    | 1              | 0.1                 | 0.7                       | 0.8                   |
| 2           | 1 -1 0  | 1000                   | 1              | 0.1                 | 1.4                       | 1.1                   |
| 3           | -1 1 0  | 500                    | 7              | 0.1                 | 1.3                       | 1                     |
| 4           | 1 1 0   | 1000                   | 7              | 0.1                 | 1.4                       | 1.25                  |
| 5           | -1 0 -1 | 500                    | 4              | 0                   | 0.65                      | 0.7                   |
| 6           | 1 0 -1  | 1000                   | 4              | 0                   | 1.1                       | 1.1                   |
| 7           | -1 0 1  | 500                    | 4              | 0.2                 | 1.2                       | 1.9                   |
| 8           | 1 0 1   | 1000                   | 4              | 0.2                 | 1.3                       | 1                     |
| 9           | 0 -1 -1 | 750                    | 1              | 0                   | 0.6                       | 0.7                   |
| 10          | 0 1 -1  | 750                    | 7              | 0                   | 1.2                       | 1.1                   |
| 11          | 0 -1 1  | 750                    | 1              | 0.2                 | 1.1                       | 0.95                  |
| 12          | 0 1 1   | 750                    | 7              | 0.2                 | 1.2                       | 1.05                  |
| 13          | 0 0 0   | 750                    | 4              | 0.1                 | 1                         | 1.3                   |
| 14          | 0 0 0   | 750                    | 4              | 0.1                 | 0.95                      | 1.35                  |
| 15          | 0 0 0   | 750                    | 4              | 0.1                 | 1                         | 1.3                   |



**Figure 10.** Comparison of results obtained from finite element model and mathematical model for HAZ size.



**Figure 11.** Comparison of results obtained from finite element model and mathematical model for SZ+TMAZ size.

that there is an acceptable agreement between the results.

The experimental data are used to validate the results of the mathematical model achieved by the RSM. For this purpose, three different cases are randomly selected in the range of experiments, and the results of the mathematical model are compared with those obtained by the measurements. The comparisons for SZ+TMAZ and HAZ sizes are presented in Table 8 and Table 9, respectively. As it can be seen from the error values given in these tables, the maximum error is 0.1 mm (9%) which indicates a good agreement between the results.

### 3.6. Effect of the welding parameters on the size of the weld zones

Figure 12 shows the direct impact of the welding parameters: rotational speed, dwell time, and plunging depth on the size of SZ+TMAZ and HAZ. As it can be seen in Fig. 12a, the size of SZ+TMAZ increases by increasing the rotational speed, plunging depth and dwell time. By increasing these parameters, the amount of input heat to the work-piece increases and the stirring effect around the pin intensifies and leads to a larger size of SZ+TMAZ. It is clear that the impact of the rotational speed on the size of SZ+TMAZ at very low

**TABLE 8.** Experimental and mathematical model results for the thickness of SZ+TMAZ

|  | Rotational speed (rpm) | Dwell time (s) | Plunging depth (mm) |                    | Error (%)   |
|--|------------------------|----------------|---------------------|--------------------|-------------|
|  |                        |                | Experimental        | Mathematical model |             |
|  | 600                    | 0.5            | 0.15                | 1.1                | 1.09 (0.9%) |
|  | 800                    | 2              | 0.1                 | 0.9                | 0.97 (7.7%) |
|  | 900                    | 1              | 0.05                | 1                  | 1.02 (2%)   |

**TABLE 9.** Experimental and Mathematical model results for the thickness of HAZ

|  | Rotational speed (rpm) | Dwell time (s) | Plunging depth (mm) |                    | Error (%)    |
|--|------------------------|----------------|---------------------|--------------------|--------------|
|  |                        |                | Experimental        | Mathematical model |              |
|  | 600                    | 0.5            | 0.15                | 1.2                | 1.15 (4.16%) |
|  | 800                    | 2              | 0.1                 | 1.4                | 1.32 (7.14%) |
|  | 900                    | 1              | 0.05                | 1.1                | 1 (9%)       |

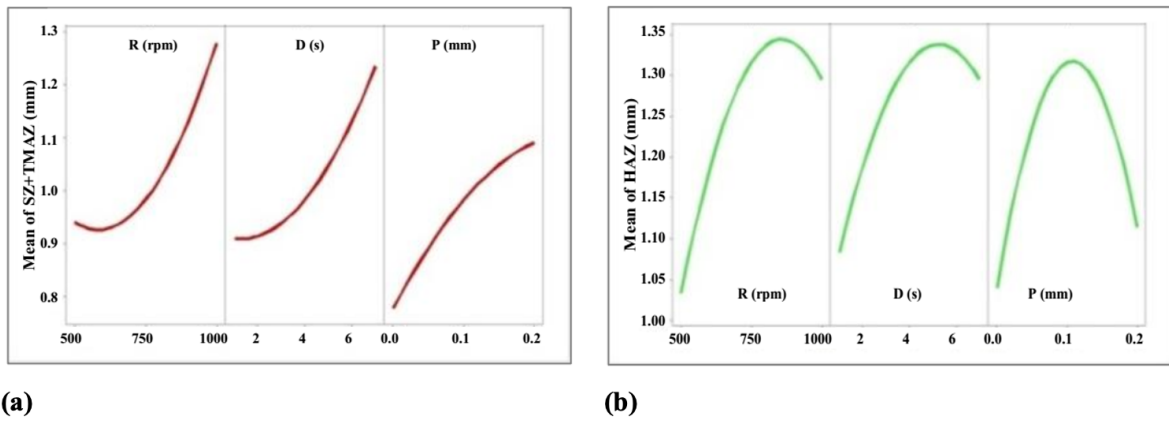


**Figure 12.** The impact of the parameters, rotational speed, dwell time and plunging depth on the size of weld zones for a) SZ+TMAZ b) HAZ.

revolutions (from 500 rpm to 550 rpm) is insignificant. This figure also shows that the increase of the SZ+TMAZ size by increasing the plunging depth is lower than the increase of the size of this area by increasing other parameters. In Fig. 12b it is evident that by increasing the rotational speed, the size of HAZ increases to a maximum value and then decreases. By increasing the rotational speed, the temperature increases and that causes the HAZ size to enlarge, but with further increase of this parameter, HAZ size decreases because the amount of stirring increase and SZ+TMAZ moves outward and replaces the HAZ.

The impact of the dwell time on the HAZ size is similar to the impact of the rotational speed. Initially, the size of HAZ rises to a maximum amount and then is reduced due to the enlargement of the SZ+TMAZ. The trend of change of the HAZ size due to the increase in the plunging depth is similar to the other parameters.

In addition to the direct effect of parameters on the size of different zones, the interference effect of parameters is also very important. Figure 13 shows the interference effect of the parameters on SZ+TMAZ size. According to Fig. 13(a), at low rotational speeds, due to the increase in the plunging depth, the size of

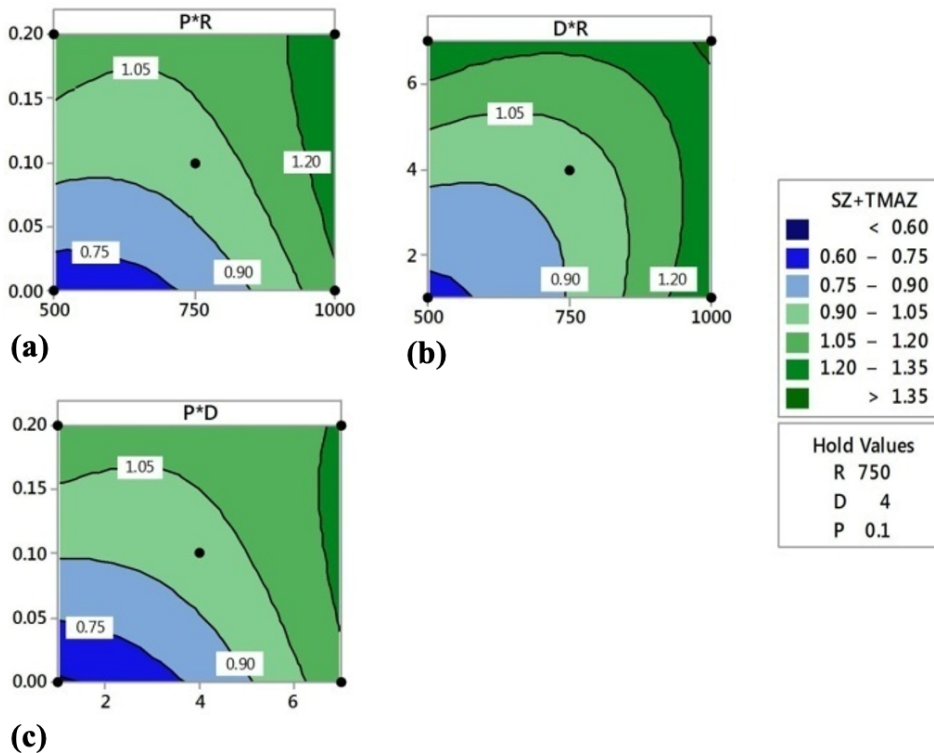


**Figure 13.** Interference effect of parameters on SZ+TMAZ size, a) plunging depth and rotational speed, b) dwell time and rotational speed, and c) plunging depth and dwell time.

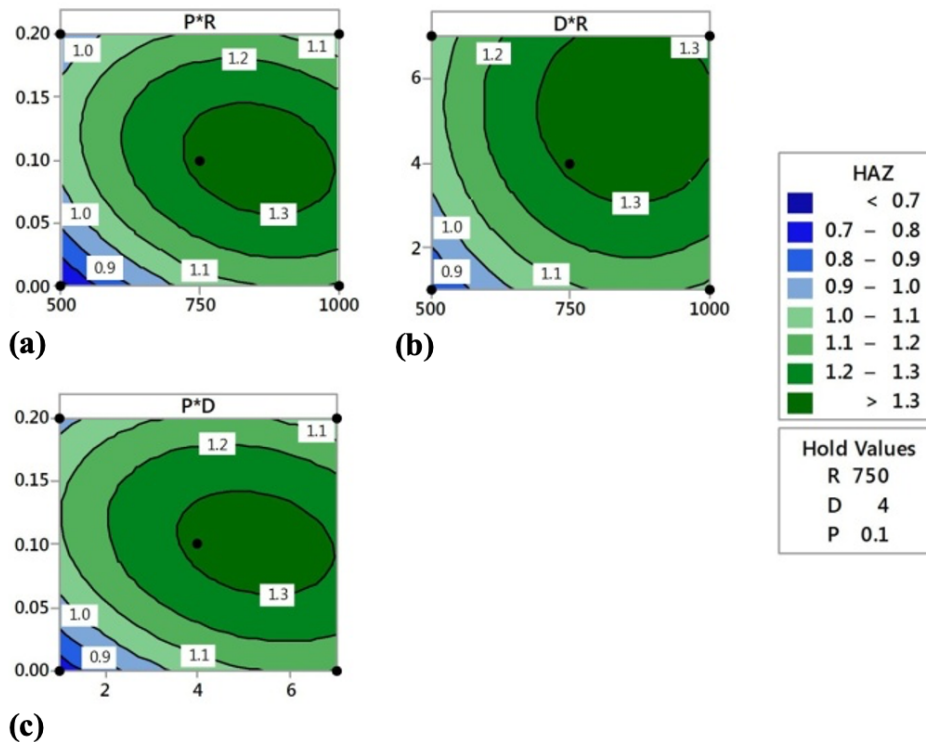


**Figure 14.** Interference effect of parameters on HAZ size, a) plunging depth and rotational speed, b) dwell time and rotational speed, and c) plunging depth and dwell time.

SZ+TMAZ rises. The increase rate of SZ+TMAZ size is reduced by raising the rotational speed. However, by reaching a speed of 750 rpm, the increase rate of size for this zone rises. Actually, at speeds greater than 750 rpm, the effect of increasing the plunging depth is greater and causes a faster growth in this zone. Fig. 13 (b-c) show the interaction between the dwell time and the rotational speed. As it is seen, by increasing of these two parameters at the same time, the size of SZ+TMAZ increases. This rate, at speeds lower than 750 rpm, is low and at speeds greater than 850 rpm is high. Actually, the simultaneous effect of these two parameters is much greater in higher values. Since the rotational speed and the dwell time have the same direct effect on the size of SZ+TMAZ, the interference effect of the dwell time and the plunging depth is similar to the interference effect of the rotational speed and the plunging depth.

Figure 14a shows the interference effect of the plunging depth and the rotational speed parameters on HAZ size. The maximum value of this zone occurs when the rotation speed is between 750 and 1000 rpm and the plunging depth is between 6.0 and 14.0 mm. At lower values than these ranges, the HAZ size is reduced due to the lower input heat. Besides, at higher values than these ranges, the HAZ size is reduced because of SZ expansion. Figure 14 (b-c) show that the highest value of the HAZ size occurs when the rotational speed

is between 750 and 1000 rpm and the dwell time is between 3.5 and 7 s due to the interference effect between the rotation speed and the dwell time. Due to the same direct effect of the rotating speed and the dwell time, the interference effect of the dwell time and the plunging depth is similar to the interfering effect of the rotating speed and the plunging depth on the size of the HAZ zone.

#### 4. CONCLUSIONS

In this paper the effect of the rotational speed, the plunging depth and the dwell time on the size of weld zones in FSSW of 304L SS plates are studied. The impact of these parameters is assessed via DOE by RSM. Using the variance analysis, the direct, the second degree and the interacting effect of parameters on the output of the process are considered. The test conditions are defined by the RSM and to reduce the number tests and consequent expenses, after validation, the FE based numerical solutions are employed. The results are summarized as follows:

- Based on the RSM two relationships are developed that can be used to predict the weld zone sizes as a function of the welding parameters.
- It has been shown that the size of SZ increases by increasing the magnitude of the welding parameters.

- When the plunging depth is constant and equal to 0.1 mm and the rotational speed is at the range of 950 to 1000 rpm and the dwell time is in the range of 6 to 7 s, the largest HAZ size is obtained.
- When the dwell time is constant and equal to 4 s and the rotational speed is in the range of 950 rpm to 1000 rpm and the plunging depth is in the range of 0.1 to 0.2 mm, the largest SZ+TMAZ size is achieved.
- The largest HAZ size occurs at the range of 750 to 1000 rpm and 0.06 to 0.14 mm for the rotational speed and the plunging depth, respectively.

## REFERENCES

- Abaqus Version 6.14 (2014). User's Manual, Dassault Systemes, Simulia Corp.; Providence, RI, USA.
- Ahmed, M.M.Z., Ahmed, E., Hamada, A.S., Khodir, S.A., Seleman, M.E.S., Wynne, B.P. (2016). Microstructure and mechanical properties evolution of friction stir spot welded high-Mn twinning-induced plasticity steel. *Mater. Des.* 91, 378-387. <https://doi.org/10.1016/j.matdes.2015.12.001>.
- Al-Moussawi, M., Smith, A.J., Faraji, M. (2017). Friction stir welding of EH46 steel grade at dwell stage: Microstructure evolution. *Metallogr. Microstruct. Anal.* 6, 489-501. <https://doi.org/10.1007/s13632-017-0390-5>.
- ASTM E3-01 (2001). *Standard Practice for Preparation of Metallographic Specimens*. ASTM International, West Conshohocken, PA, USA. <https://doi.org/10.1520/E0003-01>
- ASTM E384 (2017). *Standard Test Method for Microindentation Hardness of Materials*. ASTM International, West Conshohocken, PA, USA. <https://doi.org/10.1520/E0384-17>.
- Aota, K., Ikeuchi, K. (2009). Development of friction stir spot welding using rotating tool without probe and its application to low-carbon steel plates. *Weld. Int.* 23 (8), 572-580. <https://doi.org/10.1080/09507110802543054>.
- Avinash, P., Manikandan, M., Arivazhagan, N., Devendranath Ramkumar, K., Narayanan, S. (2014). Friction Stir Welded Butt Joints of AA2024 T3 and AA7075 T6 Aluminum Alloys. *Procedia Eng.* 75, 98-102. <https://doi.org/10.1016/j.proeng.2013.11.020>.
- Awang, M. (2007). *Simulation of friction stir spot welding (FSSW) process: Study of friction phenomena*. ProQuest, Graduate Theses, Dissertations, and Problem Reports. 8426, West Virginia University. <https://researchrepository.wvu.edu/etd/8426>.
- Bang, H.S., Lee, W.R., Hong, S.M., Lee, S.Y., Song, J.H., Kim, J.M., Bang, H.S. (2018). Mechanical Properties of Dissimilar A356/SAPH440 Lap Joints by the Friction Stir Spot Welding and Self-Piercing Riveting. *Strength Mater.* 50, 63-71. <https://doi.org/10.1007/s11223-018-9943-3>.
- Heidarzadeh, A., Saeid, T. (2013). Prediction of mechanical properties in friction stir welds of pure copper. *Mater. Des.* 52, 1077-1087. <https://doi.org/10.1016/j.matdes.2013.06.068>.
- Heidarzadeh, A., Mironov, S., Kaibyshev, R., Çam, G., Simar, A., Gerlich, A., Khodabakhshi, F., Mostafaei, A., Field, D.P., Robson, J.D., Deschamps, A., Withers, P.J. (2021). Friction stir welding/processing of metals and alloys: A comprehensive review on microstructural evolution. *Prog. Mater. Sci.* 117, 100752. <https://doi.org/10.1016/j.pmatsci.2020.100752>.
- Hirasawa, Sh., Badarinarayan, H., Okamoto, K., Tomimura, T., Kawanami, T. (2010). Analysis of effect of tool geometry on plastic flow during friction stir spot welding using particle method. *J. Mater. Process. Technol.* 210 (11), 1455-1463. <https://doi.org/10.1016/j.jmatprotec.2010.04.003>.
- Jiji, L.M. (2006). *Heat Convection*. Springer-Verlag Berlin Heidelberg. <https://doi.org/10.1007/978-3-540-30694-8>.
- Johnson, G.R., Cook, J.R. (1983). Constitutive model and data for metals subjected to large strains, high strain rates and high temperatures. Proceedings of 7th Symposium on Ballistics. (Netherlands), pp. 541-547.
- Khedr, M., Hamada, A., Järvenpää, A., Elkhatatny, S., Abd-Elaziem, W. (2023). Review on the Solid-State Welding of Steels: Diffusion Bonding and Friction Stir Welding Processes. *Metals* 13 (1), 54. <https://doi.org/10.3390/met13010054>.
- Khuri, A.I., Mukhopadhyay, S. (2010). Response surface methodology. *Wiley Interdiscip. Rev. Comput. Stat.* 2 (2), 128-149. <https://doi.org/10.1002/wics.73>.
- Kokawa, H., Park, S.H.C., Sato, Y.S., Okamoto, K., Hirano, S., Inagaki, M. (2005). Microstructures and properties of friction stir welded 304 austenitic stainless steel. *Weld. World* 49, 34-40. <https://doi.org/10.1007/BF03266473>.
- Kondapalli, S.P., Rao, Ch. S., Rao, D.N. (2014). A Review on Welding of AISI 304L Austenitic Stainless Steel. *J. Manuf. Sci. Prod.* 14 (1), 1-11. <https://doi.org/10.1515/jmsp-2012-0007>.
- Lakshminarayanan, A.K., Annamalai, V.E., Elangovan, K. (2015). Identification of optimum friction stir spot welding process parameters controlling the properties of low carbon automotive steel joints. *J. Mater. Res. Technol.* 4 (3), 262-272. <https://doi.org/10.1016/j.jmrt.2015.01.001>.
- Maurel-Pantel, A., Fontaine, M., Thibaud, S., Gelin, J.C. (2012). 3D FEM simulations of shoulder milling operations on a 304L stainless steel. *Simul. Model. Pract. Theory* 22, 13-27. <https://doi.org/10.1016/j.simpat.2011.10.009>.
- Mishra, R.S., Ma, Z.Y. (2005). Friction Stir Welding and Processing. *Mater. Sci. Eng. R Rep.* 50 (1-2), 1-78. <https://doi.org/10.1016/j.mser.2005.07.001>.
- Mishra, R.S. (2008). Preface to the Viewpoint Set on friction stir processing. *Scr. Mater.* 58 (5), 325-326. <https://doi.org/10.1016/j.scriptamat.2007.10.044>.
- Mohan, D.G., Wu, Ch.S. (2021). A Review on Friction Stir Welding of Steels. *Chin. J. Mech. Eng.* 34, 137. <https://doi.org/10.1186/s10033-021-00655-3>.
- Park, S.C., Sato, Y.S., Kokawa, H., Okamoto, K., Hirano, S., Inagaki, M. (2003). Rapid formation of the sigma phase in 304 stainless steel during friction stir welding. *Scr. Mater.* 49 (12), 1175-1180. <https://doi.org/10.1016/j.scriptamat.2003.08.022>.
- Ragab, M., Liu, H., Yang, G.J., Ahmed, M.M.Z. (2021). Friction Stir Welding of 1Cr11Ni2W2MoV Martensitic Stainless Steel: Numerical Simulation Based on Coupled Eulerian Lagrangian Approach Supported with Experimental Work. *Appl. Sci.* 11 (17), 3049. <https://doi.org/10.3390/app11073049>.
- Ravi Sekhar, S., Chittaranjandas, V., Govardhan, D., Karthikeyan, R. (2018). Effect of tool rotational speed on friction stir spot welded AA5052-H38 aluminum alloy. *Mater. Today: Proc.* 5 (2), 5536-5543. <https://doi.org/10.1016/j.matpr.2017.12.144>.
- Reilly, A., Shercliff, H., Chen, Y., Prangnell, Ph. (2015). Modeling and visualization of material flow in friction stir spot welding. *J. Mater. Process. Technol.* 225, 473-484. <https://doi.org/10.1016/j.jmatprotec.2015.06.021>.
- Reynolds, A.P., Tang, W., Gnaupel-Herold, T., Prask, H. (2003). Structure, properties and residual stress of 304L stainless steel friction stir welds. *Scr. Mater.* 48 (9), 1289-1294. [https://doi.org/10.1016/S1359-6462\(03\)00024-1](https://doi.org/10.1016/S1359-6462(03)00024-1).
- Salih, O.S., Ou, H., Sun, W. (2023). Heat generation, plastic deformation and residual stresses in friction stir welding of aluminium alloy. *Int. J. Mech. Sci.* 238, 107827. <https://doi.org/10.1016/j.ijmecsci.2022.107827>.
- Siddiquee, A.N., Pandey, S., Zaman Khan, N. (2015). Friction Stir Welding of Austenitic Stainless Steel: A Study on Microstructure and Effect of Parameters on Tensile Strength. *Mater. Today: Proc.* 2 (4-5), 1388-1397. <https://doi.org/10.1016/j.matpr.2015.07.058>.
- Siddiquee, A.N., Pandey, S., Abidi, M.H., Al-Ahmari, A., Khan, N.Z., Gangil, N. (2020). Microstructural characterization and in-process traverse force during friction stir welding of austenitic stainless steel. *Proc. Inst. Mech. Eng., Part C* 234 (5), 1031-1043. <https://doi.org/10.1177/0954406219888238>.
- Sharabeyani, S., Daei Sorkhabi, A.H. (2022). The effects of rotational and traverse speeds and SiC particles on the microstructure and mechanical properties of AA 5052 in friction stir welding. *Int. J. Mater. Res.* 113 (2), 149-160. <https://doi.org/10.1515/ijmr-2020-8038>.
- Vakili Tahami, F., Daei Sorkhabi, A.H., Biglari, F.R. (2010). Creep constitutive equations for cold-drawn 304L stainless steel. *Mater. Sci. Eng. A* 527 (18-19), 4993-4999. <https://doi.org/10.1016/j.msea.2010.04.055>.

- Verma, S., Kumar, V., Kumar, R., Sidhu, R.S. (2022). Exploring the application domain of friction stir welding in aluminum and other alloys. *Mater. Today: Proc.* 50 (5), 1032-1042. <https://doi.org/10.1016/j.matpr.2021.07.449>.
- Vinayak, M., Sanjeev, N.K., Suresh Hebbar, H., Kailas, S.V. (2014). Time Efficient Simulations of Plunge and Dwell Phase of FSW and its Significance in FSSW. *Procedia Materials Science* 5, 630-639. <https://doi.org/10.1016/j.mspro.2014.07.309>.
- Zhu, X.K., Chao, Y.J. (2004). Numerical simulation of transient temperature and residual stresses in friction stir welding of 304L stainless steel. *J. Mater. Process. Technol.* 146 (2), 263-272. <https://doi.org/10.1016/j.jmatprotec.2003.10.025>